

SENSITIVE VLA OBSERVATIONS OF OH 127.8–0.0 AND OH 26.5+0.6

P. F. BOWERS¹

Sachs/Freeman Associates, Inc.

AND

K. J. JOHNSTON

E. O. Hulburt Center for Space Research, Naval Research Laboratory

Received 1989 July 3; accepted 1989 November 10

ABSTRACT

VLA maps with the highest signal-to-noise ratio and dynamic range thus far observed for OH/IR stars are presented throughout the velocity range of the outer envelopes for the bright 1612 MHz sources OH 127.8–0.0 and OH 26.5+0.6. The maps are compared to VLBI and MERLIN data, and the shell parameters are determined to the highest accuracy obtainable with the assumptions of the standard expanding shell model. The linear radius of the maser shell of OH 127.8–0.0 is constant to within $\pm 10\%$ (rms) as a function of direction from the star, but that of OH 26.5+0.6 differs by as much as 50% on opposite sides of the shell, possibly because of excess ultraviolet radiation contributed by an O8 star in its vicinity. We consider the extent to which rotational components, radial acceleration, or random velocity fluctuations may be present in the envelopes. OH 127.8–0.0 appears to be a supergiant star, but its OH profile and light curve are unlike those of known supergiants.

Subject headings: infrared: sources — interferometry — masers — stars: circumstellar shells

I. INTRODUCTION

High-spatial resolution observations of the 1612 MHz OH emission associated with OH/IR stars reveal a hierarchy of sizes for structural features. VLBI measurements indicate occasional maser components with sizes less than $0''.05$ (Reid *et al.* 1977; Bowers *et al.* 1980; Norris *et al.* 1984). Shorter baseline MERLIN measurements commonly show components at about the $0''.1$ – $0''.3$ level which are distributed over partial ringlike structures (e.g., Booth *et al.* 1981; Diamond *et al.* 1985). Complete ringlike structures with angular diameters of a few arcseconds are detected with the VLA and are typically composed of several unresolved ($< 1''$) clumps intermixed with relatively smooth regions of comparable size (Bowers, Johnston, and Spencer 1983, hereafter BJS; Herman *et al.* 1985; Welty, Fix, and Mutel 1987).

It is likely that the map structure is determined by a combination of density/velocity effects, making the interpretive link between the observed maser distribution and the underlying envelope structure difficult to establish uniquely. Regions of maser clumping are not necessarily regions where the mass density is higher. The large-scale ($1''$) clumping seen in the VLA maps may represent regions of larger OH density if the three-dimensional shape of the shell is spherical (BJS; Herman *et al.* 1985), or regions of longer velocity-coherent path lengths if the shape is aspherical (Bowers, Johnston, and de Vegt 1989, hereafter BJDV). The map structure may also be influenced by anisotropies in the ambient UV radiation field (Huggins and Glassgold 1982; Netzer and Knapp 1987; Szymczak 1987), or by random nonradial velocity fluctuations which can destroy the velocity-coherent path lengths required for the maser emission (Deguchi 1982). The small-scale ($0''.1$) clumps (or maser spots) commonly seen in MERLIN and VLBI maps may be the result of such velocity fluctuations, but interpretation of the maps is further complicated by the possibility that the maser

emission arises from platelike structures or blobs (Alcock and Ross 1986) rather than from smooth, windlike flow (Sun and Kwok 1987).

Despite these complexities, the maser maps for most OH/IR stars provide reasonable agreement, to a first-order approximation, with the predictions of the standard expanding shell model in the outer envelopes ($R_s > 1000$ AU). The model assumes that the gas in the maser region is uniformly distributed in a thin shell with a constant outflow velocity in all directions. This results in a doubly peaked profile and an angular radius θ of the emission distribution which depends on the velocity V by the parabolic relation

$$\theta = \theta_s [1 - (V - V_0)^2 / V_e^2]^{1/2}, \quad (1)$$

where θ_s is the shell radius, V_0 is the stellar radial velocity, and V_e is the radial expansion velocity (Kwok 1976; Elitzur, Goldreich, and Scoville 1976; Reid *et al.* 1977).

The clumpy nature of the maser maps and various differences between the observed and predicted $\theta(V)$ relationships and profile structures are reminders that the standard model is only an approximation (Bowers 1985; BJDV). A key to understanding the nature of these differences is to obtain high-quality interferometric data throughout the entire velocity range of the envelope. In this paper we present the results of VLA observations with a much higher signal-to-noise ratio and dynamic range than previously has been observed for the bright OH/IR stars OH 127.8–0.0 (= OH 127) and OH 26.5+0.6 (= OH 26.5). Both stars have continuous emission between the outer peaks, and maps are presented at all velocities. OH 127 has one of the best-known examples of a spherically shaped shell yet found for an OH/IR star, allowing us to estimate for an optimum case the level at which errors for the determination of the shell parameters are limited by deviations from the standard shell model. The shell of OH 26.5 is one of the least symmetric known for OH/IR stars. It is possible that much of the asymmetry is caused by anisotropic UV radiation.

¹ Work performed at NRL under contract number N00014-88C-2475.

II. OBSERVATIONS AND DATA REDUCTION

During 1985 January 19, data for OH 127 were obtained by using the NRAO² Very Large Array and the observational setup described by BJDV. These data provided a profile with high-velocity resolution ($\Delta V = 0.28 \text{ km s}^{-1}$ at 1612.231 MHz) near maximum light ($\phi = 0.16$ from the OH light curve of Herman and Habing 1985), and also allowed us to determine positions of peak and extreme velocity profile features in order to ensure that the positions (and map structures) are not radically affected by the velocity resolution. The results are discussed in § III.

VLA observations with much higher sensitivity but poorer velocity resolution were subsequently obtained for OH 127 and OH 26.5 during 1986 March 8, using 18 antennas in the A-configuration with baselines which ranged from 0.8 to 36.6 km. The phases ϕ of the light curves were 0.61 for OH 127 and 0.38 for OH 26.5. The effective bandpass (391.25 kHz) was divided into 64 channels and on-line Hanning smoothing was applied to the data, resulting in a resolution and channel-to-channel separation of 6.1 kHz ($\Delta V = 1.14 \text{ km s}^{-1}$) and an effective velocity coverage of 72 km s^{-1} . The sources were observed in the right-handed circular polarization mode for both epochs.

The unresolved continuum sources 0107+562 and 1741–038 were used to calibrate the amplitudes and phases of the visibility data for OH 127 and OH 26.5, respectively, from an observing sequence which consisted of 25 minute on-source observations interleaved with 5 minute calibrator observations. The total on-source integration time was 4.8 hr for OH 127 and 3.2 hr for OH 26.5. The flux density scale was established from an observation of 3C 286 with an adopted flux density of 13.83 Jy. The derived flux densities were 1.79 ± 0.01 Jy for 0107+562 and 2.00 ± 0.02 Jy for 1741–038.

Maps of the calibrated visibility data were made for each channel with uniform weighting in the u - v plane. The maps were then cleaned and restored with a circular Gaussian beam of full width at half-maximum (FWHM) extent equal to $1''$. To increase the dynamic range of the maps of the stronger emission features, a subsequent set of maps was made in which a self-calibration algorithm was applied. The maps of OH 127 were phase-referenced to the emission at -65.3 km s^{-1} , and those of OH 26.5 were referenced to the emission at 13.3 km s^{-1} . Despite the self-calibration procedure, maps of the stronger emission features are still dynamic range-limited. The dynamic range is approximately 400:1 for OH 127 and 200:1 for OH 26.5. The remaining maps are limited by the signal-to-noise ratio. For these maps, the lowest contour level is 18 mJy per beam for OH 127 and 25 mJy per beam for OH 26.5, corresponding approximately to 2.5 times the root mean square (rms) noise level (σ) of the appropriate map.

III. RESULTS AND ANALYSIS

a) OH 127.8–0.0 (AFGL 230; IRAS 01304+6211)

i) Map Structure

Maps of the 1612 MHz emission distribution throughout the entire velocity range of the envelope are shown in Figure 1. Emission between -60.7 and -50.4 km s^{-1} has not previously been mapped. The structure is dominated at virtually

all velocities by a relatively strong eastern component, indicating an edge-on, continuous ringlike structure in that portion of the shell. Weaker clumps of emission at other position angles are evident near the midpoint (-55 km s^{-1}) of the velocity range, where the shell size is largest, and they persist over velocity intervals of about 4 km s^{-1} . At some velocities (e.g., -50.4 km s^{-1}), the emission distribution between the clumps is relatively smooth over a scale size exceeding $1''$.

The 1612 MHz emission has been observed with a variety of spatial resolutions ranging from VLBI measurements (Bowers *et al.* 1980; Norris *et al.* 1984) to intermediate baseline measurements obtained with MERLIN (Booth *et al.* 1981; Norris, Diamond, and Booth 1982) to shorter baseline measurements made with the VLA by Bowers, Johnston, and Spencer (1981, 1983) and in this paper. A composite of these data is shown in Figure 2 along with the spectral line profiles obtained from both VLA data sets (§ II).

The VLBI map of the low-velocity peak feature (Fig. 2a) indicates that 90% of the flux originates from a compact ($< 0''.04$) component, while the remaining flux is distributed as a weak extension to the northeast. All other VLBI components in this source have sizes greater than $0''.1$. Norris *et al.* (1984) suggest that the compact component may be amplifying the stellar thermal emission.

Figure 2c represents the first interferometric detection of the low-level emission near the stellar velocity of $V_0 = -55 \text{ km s}^{-1}$. Individual channels do not show a complete shell, but this may be because the data are signal-to-noise-limited. The map in Figure 2c is an average of the central seven channels in Figure 1 ($V_0 \pm 3.4 \text{ km s}^{-1}$). This map clearly indicates a complete but clumpy ring structure which is approximately circular relative to the map origin. Small deviations from circularity are evident for the low-level contours.

Figures 2b and 2d offer a direct comparison of data obtained with MERLIN and with the VLA at two intermediate velocities symmetric to the stellar radial velocity. The small-scale (dark) contours are MERLIN data ($0''.3$ resolution) superposed on the VLA ($1''$) data. The velocities have been chosen to be as close as possible to V_0 and also to have at least several clumps of emission which were detected with the less sensitive MERLIN observations.

These maps clearly demonstrate the complementarity of observations obtained with different spatial resolutions. The higher resolution MERLIN data show the eastern component to be composed of unresolved features whose distribution agrees well with that of the stronger emission in the VLA maps. The MERLIN data show no indication of emission in the western portion of the shell. This result indicates either that the low-level emission to the west is sufficiently extended ($> 0''.3$) that it is not detected by MERLIN or, more likely, that this emission is similarly composed of small-scale clumps whose intensity is below the detection threshold of the MERLIN observations [see § IIIb(i)]. It is unlikely that the differences between the data sets are caused by temporal changes of the emission distributions. There is good correspondence of the stronger VLA features with the MERLIN data and also of features in the present maps (Fig. 1) with those seen in the earlier VLA data of BJS.

ii) Stellar Position

Conclusions concerning the shell structure are critically dependent on the adopted stellar position. Various methods previously have been used to estimate the stellar position from

² The National Radio Astronomy Observatory is operated by Associated Universities, Inc., under cooperative agreement with the National Science Foundation.

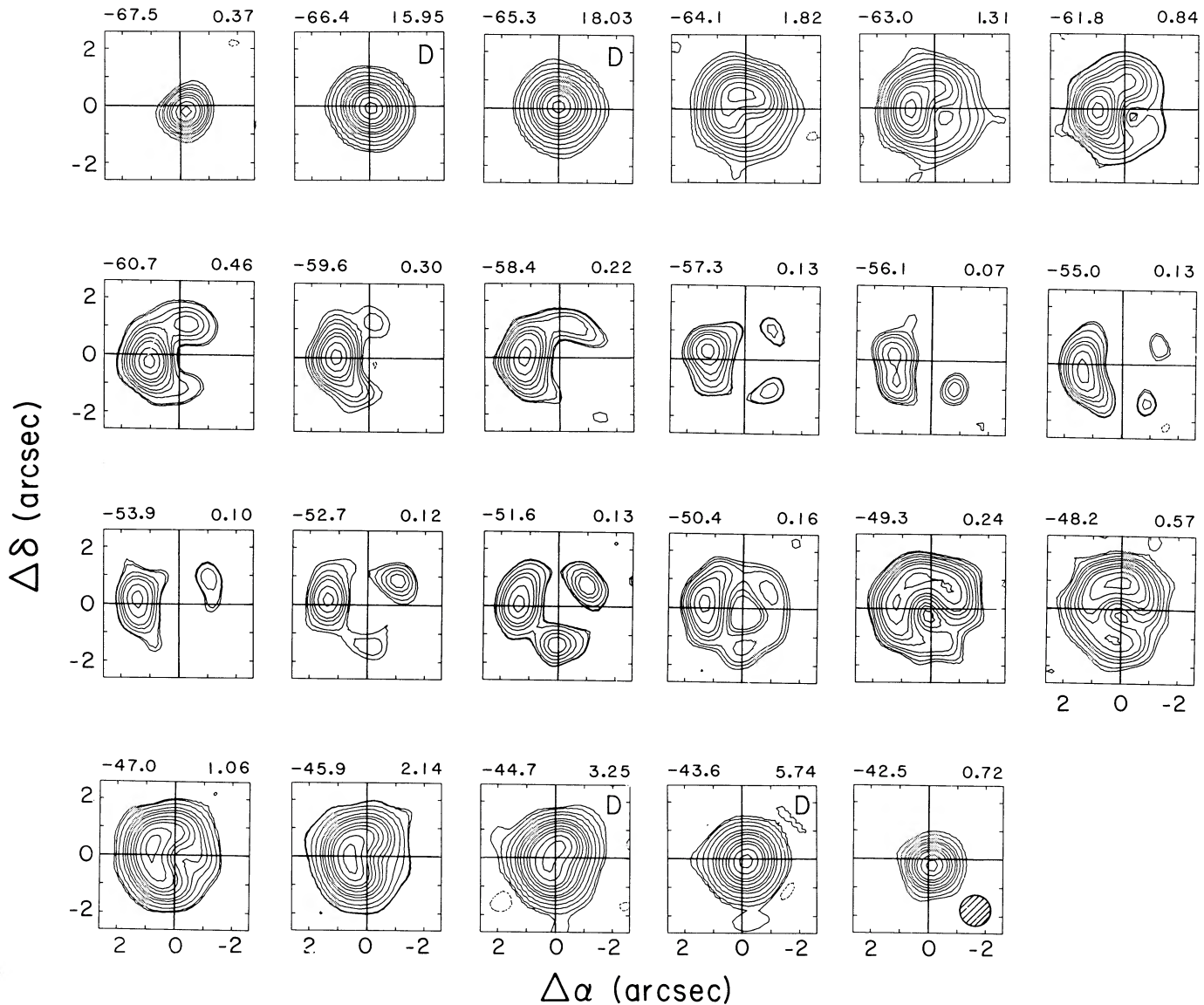


FIG. 1.—Maps of the angular distribution of 1612 MHz emission for OH 127.8–0.0 at epoch 1986.18. The origin of each map is located at $\alpha = 01^{\text{h}}30^{\text{m}}27^{\text{s}}.63$, $\delta = +62^{\circ}11'31''.20$ (epoch 1950), which represents the approximate position of the -65.8 km s^{-1} unresolved VLBI component. The LSR radial velocity (km s^{-1}) and peak flux density (Jy per beam) are indicated on each map, and the full width half-power synthesized beam is shown on the last map in the series. Contour levels are 90%, 70%, 50%, 40%, 30%, 20%, 15%, 10%, 5%, 2.5%, 1.0%, 0.5%, and -0.5% of the peak flux density for maps which are dynamic range-limited, as indicated by the “D” in the upper right corner. The lowest contour levels for maps which are noise-limited are $\pm 18 \text{ mJy per beam}$.

OH data. These include (1) the mean position of the outer peak features, (2) the mean position of the features at the most extreme low or high velocities, (3) the position of the low-velocity peak component if it is believed to be amplifying continuum emission from the stellar photosphere, and (4) least-squares fitting of equation (1) to the data for various assumed positions. These methods usually agree to within an accuracy of about $\pm 10\%$ of the shell radius θ_s , or about $\pm 0''.05$, whichever is larger. The lower limit for the error is imposed by the obtainable accuracy of the VLA measurements. Larger errors can occur because of aspherical emission distributions or nonradial motions.

Figure 3 summarizes the absolute positions of peak and extreme velocity features for three independent data sets: BJS, the maps in Figure 1 (BJ), and the VLA data obtained by

ourselves in 1985 with higher velocity resolution (Bowers and Johnston 1985, hereafter BJ85). Comparison of these data sets shows agreement of the absolute positions to within $\pm 0''.05$ after interpolation to identical velocities. The higher resolution data set (BJ85) indicates that the velocities of the peak features occur at -65.8 ± 0.15 and $-43.6 \pm 0.15 \text{ km s}^{-1}$. These features are separated by about $0''.15$ in Figure 3. The separation is $\approx 0''.05$ for the extreme velocity features.

The mean positions of the appropriate low- and high-velocity components are listed in Table 1 for all three data sets. The differences between the “average” positions determined by the three methods exceed the expected observational error and indicate deviations from the idealized expanding shell model. These differences make it difficult to determine the stellar position of this star to an accuracy better than $\pm 0''.1$

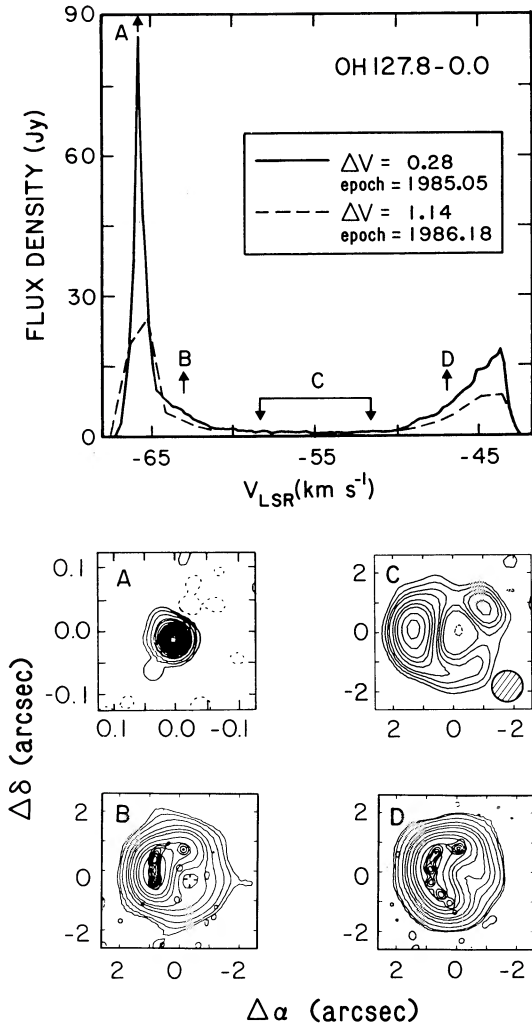


FIG. 2.—VLA spectral line profiles near maximum and minimum light and maps at selected velocities for OH 127.8-0.0. Map A is a VLBI map of the low-velocity peak feature (Norris *et al.* 1984). Maps B and D are superpositions of MERLIN data (Norris, Diamond, and Booth 1982) onto the VLA maps from Fig. 1 at velocities of -63.0 and -47.0 km s^{-1} , respectively. Map C is the average of emission from -58.4 to -51.6 km s^{-1} . Contour levels are 90%, 70%, 50%, 40%, 30%, 20%, 15%, 10%, and $\pm 5.7\%$ of the peak flux density of 0.12 Jy per beam. The origin of each map is identical to that in Fig. 1, and the FWHM VLA beam is shown in the lower right corner of map C.

and also cast some doubt on whether the compact VLBI component at $V = -65.8$ km s^{-1} is actually amplifying the stellar continuum emission.

To explore this latter point further, equation (1) was fitted to the $\theta(V)$ data by the method of least squares for various assumed positions of the star. The position of the best fit (and highest shell symmetry) is given in Table 1 and is closest to the position of the low-velocity peak (and VLBI component). We therefore adopt the mean position of the -65.8 km s^{-1} feature as the stellar position ($\alpha = 01^{\text{h}}30^{\text{m}}27^{\text{s}}.627$, $\delta = +62^{\circ}11'31''.22$; from Table 1), although it is noteworthy that this position is displaced by about $0''.1$ from both the mean position of the peak features and from that of the extreme features.

Figure 4 shows the resulting $\theta(V)$ relationships for the adopted stellar position. The angular radius θ at a given V refers to the radius of maximum emission. This parameter has been measured in this way because it can be determined over a larger range of position angles than if it is measured only at the

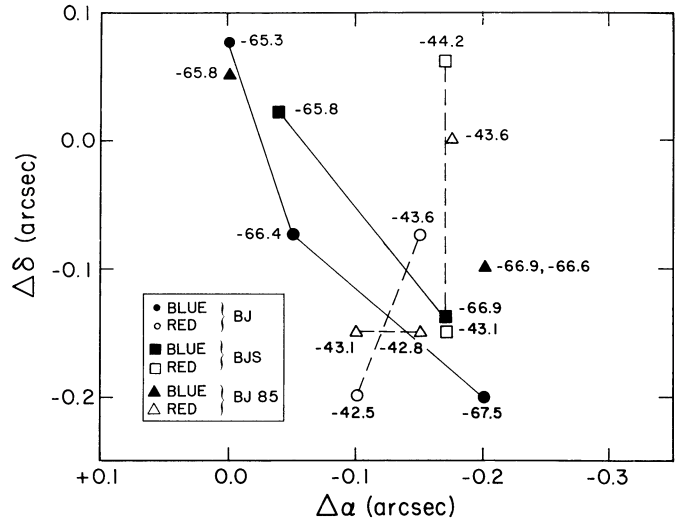


FIG. 3.—Absolute positions of emission components at the velocities of the peaks and at more extreme low or high velocities for OH 127.8-0.0. The lines connect adjacent velocities of the same data set. The references for symbols are BJ = this paper, BJS = Bowers, Johnston, and Spencer (1983), and BJ85 = unpublished data by Bowers and Johnston, epoch 1985.05. The absolute position of the origin of the map is identical to that in Fig. 1. The intrinsic error for an unresolved component is estimated to be $\pm 0''.05$.

positions of clumps. It does not account for structure seen in the lowest contour levels of the maps.

b) OH 26.5+0.6 (AFGL 2205; IRAS 18348-0526)

i) Map Structure

This source has been mapped four times with the VLA, each time with an increasingly higher sensitivity (Baud 1981; BJS. Herman *et al.* 1985; this paper, hereafter BJ). The maps are presented in Figure 5 throughout the entire velocity range of emission and show good agreement with previous maps after allowance for different sensitivities. The shell has an apparent angular size which is the largest of any OH/IR star yet mapped, and it is well resolved with the VLA. Complete ring-like structure is seen at virtually all velocities, but the shell structure is quite clumpy, with five or six clumps readily

TABLE 1
POSITION DETERMINATIONS FOR OH 127.8-0.0^a

Method	$\Delta\alpha$	$\Delta\delta$	Reference
Mean of outer peaks			
($V = -65.8; -43.6$)	$-0''.11$	$-0''.02$	BJS
	-0.08	$+0.02$	BJ85
	-0.09	-0.04	BJ
Average	-0.09	-0.01	
Mean of extrema			
($V = -66.9; -42.8$)	-0.17	-0.14	BJS
	-0.17	-0.12	BJ85
	-0.12	-0.15	BJ
Average	-0.15	-0.14	
Low-velocity peak			
($V = -65.8$)	-0.04	$+0.02$	BJS
	0.00	$+0.05$	BJ85
	-0.02	$+0.00$	BJ
Average	-0.02	$+0.02$	
Least-squares fit	-0.05	$+0.07$	BJ

^a Relative to the origin of $\alpha = 01^{\text{h}}30^{\text{m}}27^{\text{s}}.630$, $\delta = +62^{\circ}11'31''.20$ (epoch 1950.0).

REFERENCES.—BJS: Bowers, Johnston, and Spencer 1983. BJ85: Bowers and Johnston 1985. BJ: This paper (maps in Fig. 1).

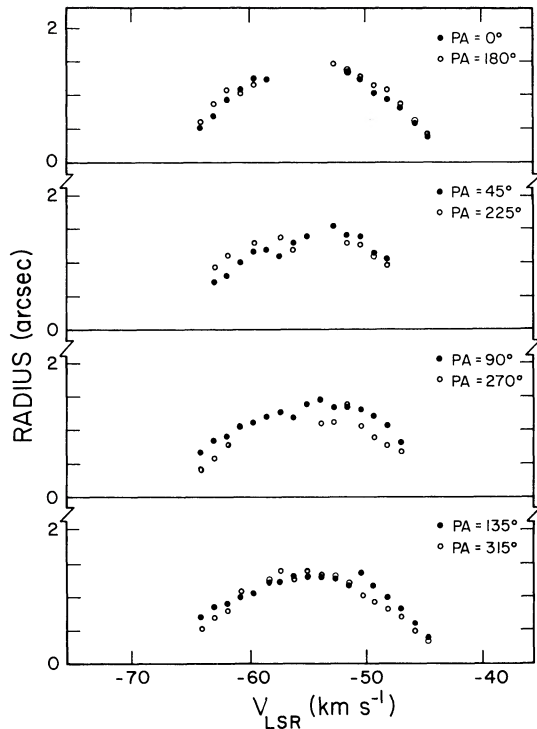


FIG. 4.—Angular distance θ of the maximum emission from the origin of the maps in Fig. 1 as a function of the position angle and the LSR radial velocity.

evident at a given velocity. At $V = 25.9 \text{ km s}^{-1}$, the structure is smooth over a scale size of about $2''$. Comparison to maps at adjacent velocities suggests that this “uniform” emission is probably composed of unresolved discrete clumps with comparable intensities. Also of interest are the decidedly noncircular shapes of the low-level contours at the extreme low or high velocities.

Figure 6 shows the spectral line profile and a comparison of the VLA maps to the MERLIN data of Diamond *et al.* (1985) at velocities symmetric to the stellar velocity. It is evident that the size of the emission region is larger at the low velocities than at the high velocities (see also Fig. 5). As with OH 127.8, there is good correspondence of the positions of knots seen in the MERLIN data with stronger emission seen in the VLA data. The superposition of the two data sets illustrates that smooth regions seen in the VLA maps appear to consist of numerous, small ($< 0.3''$) knots of comparable intensities. Figure 6a also clearly shows that the emission cannot be modeled as a thin ring at some velocities. Figure 6b shows the emission within $\pm 0.5 \text{ km s}^{-1}$ of the stellar velocity. The shape and details are similar to those in the map of Herman *et al.*, which is averaged over a 5 km s^{-1} velocity interval.

ii) Stellar Position

A single-dish profile obtained by Andersson *et al.* (1974) with a velocity resolution of 0.19 km s^{-1} indicates emission ranging from 11.9 to 42.0 km s^{-1} , with the strong peaks at 13.1 ± 0.1 and $40.9 \pm 0.1 \text{ km s}^{-1}$. The absolute positions of the peak and extreme velocity features obtained from the BJS data and the data in Figure 5 and plotted in Figure 7. An offset of about $0.05''$ in right ascension and $0.25''$ in declination is seen when the data at the two epochs are interpolated to identical velocities. The large difference in declination is probably attributable to

the more limited coverage in the u - v plane for the BJS data set and is consistent with the errors quoted by those authors. The relative positions of velocity components agree well when the data at the two epochs are compared.

The angular separation between the extreme velocity features is about $0.1''$, while the separation between the peak features is about $0.2''$ for each data set. The MERLIN data (Diamond *et al.* 1985) have a comparable velocity resolution (1.3 km s^{-1}) but better spatial resolution. Those data show complex emission distributions at the velocities of the peak features, consistent with the maps in Figure 5 and with VLBI results (Reid *et al.* 1977) which indicate no unresolved component such as that seen for OH 127. The MERLIN data indicate more compact ($\leq 0.5''$) structure and approximate positional coincidence at the most extreme velocities. We therefore adopt the mean position of these features ($\alpha = 18^{\text{h}}34^{\text{m}}52^{\text{s}}.467$, $\delta = -05^{\circ}26'36''.90$) as the most probable position of the star. We estimate the uncertainty to be about $\pm 0.1''$ due to structure in these features.

The $\theta(V)$ relationships are shown in Figure 8, where θ is again measured from the adopted stellar position to the maximum in the emission distribution at a given position angle. There is considerable asymmetry on opposite sides of the shell. In the east-west direction (P.A. = 90° and 270°), the far side (values of θ at higher velocities) is about 50% smaller than the near side (values of θ at lower velocities). The southern portion (P.A. = 180°) is about 50% smaller than the northern portion (P.A. = 0°) for both the near and far sides of the shell. Least-squares fitting of equation (1) to the data for various assumed positions of the star indicates that the shell is most symmetric if the stellar position is about $0.5''$ north of our adopted stellar position. Unlike OH 127, there is no small VLBI component which might indicate the stellar position. The $\theta(V)$ curves clearly indicate that radial expansion is dominant, so it is difficult to understand how the peak and extreme velocity features can be approximately positionally coincident but displaced from the stellar position by $0.5''$. We therefore assume that the star is located at our adopted position and that the shell structure is asymmetric.

c) Determination of Shell Parameters

Figure 9 displays the $\theta(V)$ relationship for OH 127 and OH 26.5, where each value of θ is averaged over 16 equally spaced position angles. The vertical bars indicate the minimum and maximum value of θ at a given velocity, regardless of position angle, and thus they are a crude measure of the shell thickness. The boxes represent estimates of θ near the outer velocities of the profile, where the size of the emission region is too small to obtain a reliable value of the shell size from the maps. These values are obtained from the visibility curves and represent $\theta_G/2$, where θ_G is the FWHM width of a Gaussian brightness distribution.

The smooth curves in Figure 9 indicate the least-squares fits of equation (1) to the averaged values of θ . The rms errors σ_f of the fits are $0.12''$ for OH 127 and $0.23''$ for OH 26.5, larger than the estimated $0.05''$ error for the determination of relative positions of features. It is evident that there is a significant asymmetry between the low- and high-velocity values of θ for OH 26.5. However, attempts to apply least-squares solutions independently to the low- and high-velocity data sets did not result in substantially smaller values of σ_f .

Values of V_0 and V_e obtained from the total width of the profile (V^W), the velocity separation of the peaks (V^P), and

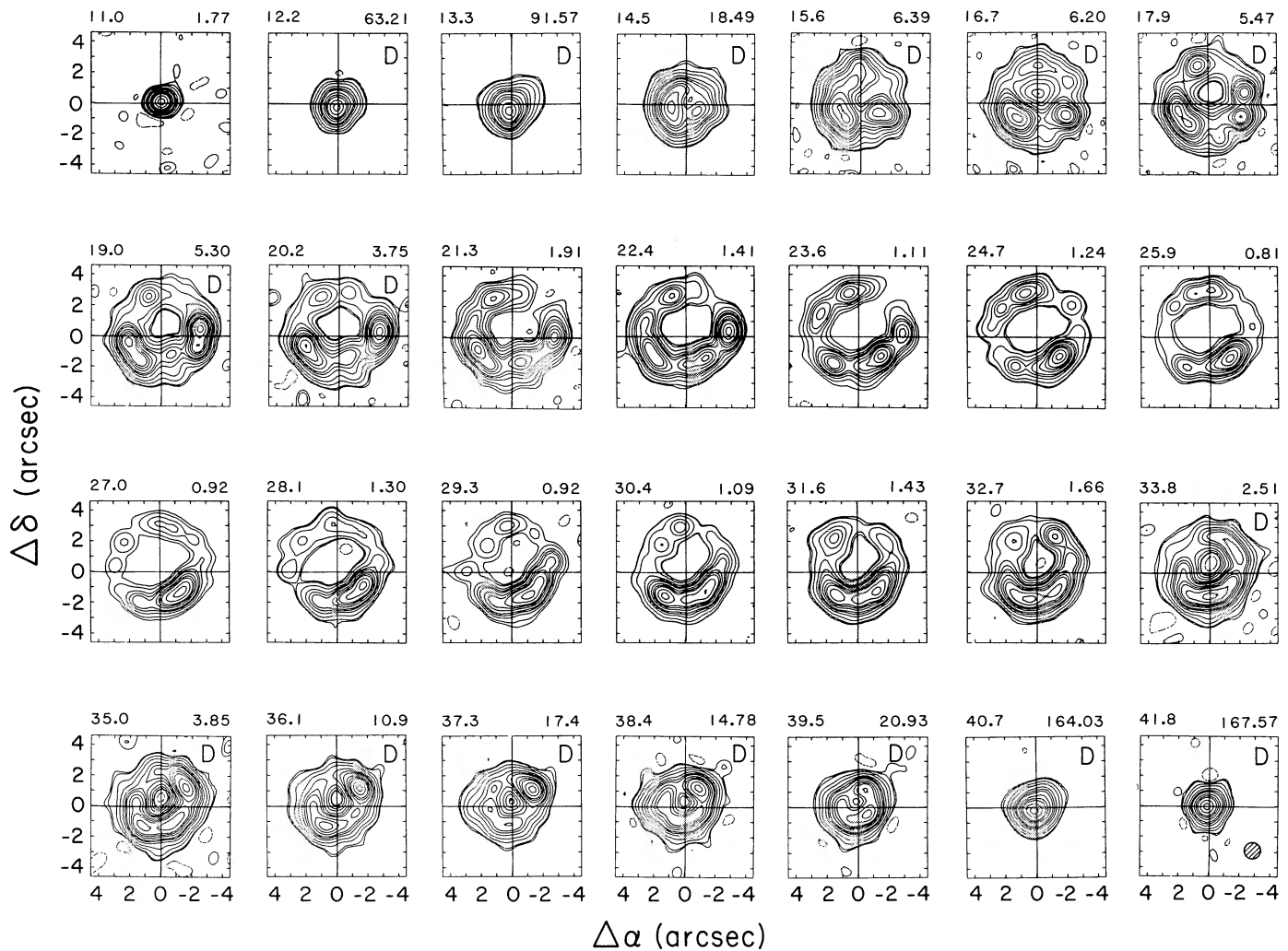


FIG. 5.—Same as Fig. 1 for OH 26.5+0.6, where the lowest contour levels are $\pm 0.7\%$ for the dynamic-range limited maps and ± 25 mJy per beam for the noise-limited maps. The origin is located at the adopted stellar position of $\alpha = 18^{\text{h}}34^{\text{m}}52^{\text{s}}.467$, $\delta = -05^{\circ}26'36''.90$ (epoch 1950).

least-squares fitting are given in Table 2. The errors for values determined from the profile represent one-half the velocity resolution; the errors associated with the least-squares fit are formal rms errors. Values of V_0 and V_e agree to within about 1 km s^{-1} for all three methods.

The values of θ_s determined from the least-squares fits also are given in Table 2 and are approximately 7% smaller than the averaged values at the stellar velocity in Figure 9. The discrepancy is likely due to deviations of the data from the assumptions implicit in the derivation of equation (1).

Figure 10 shows the individual values of θ_s as a function of position angle and illustrates the degree of asphericity of each shell in the plane of the sky. The rms fluctuation of θ_s relative to the mean value is 10% for OH 127 and 20% for OH 26.5 (Table 2). The different degrees of asphericity also can be seen from comparison of Figures 1 and 5.

The lengths of the vertical bars in Figure 10 indicate the FWHM shell thickness after deconvolution from the beam and are the first direct measures of the shell thickness at $V = V_0$. Bars are plotted only for position angles where the maximum emission exceeds 9σ , corresponding to the third contour in the

maps of Figures 1 and 5. We summarize in Table 2 the difference and ratio of the outer (θ_o) and inner (θ_i) angular radii at the level of $2 \times \text{FWHM}$. For OH 26.5 we list the minimum and maximum values and the corresponding position angles. Values of θ_o/θ_i (or equivalently R_o/R_i) are approximately one-half the upper limits estimated for these two stars by BJS but agree well with values obtained for OH Miras (BJdV).

For most OH/IR stars, it is not possible to obtain a direct measure of the shell thickness because there is little, if any, emission at the stellar velocity. In such cases, a crude measure of the ratio θ_o/θ_i can be obtained from the scatter of θ as a function of velocity (Fig. 9). We list these values in Table 2, derived from θ_{min} and θ_{max} at $V = V_0$. Comparison of the ratios derived directly and indirectly show that the indirect ($\theta_{\text{min}}, \theta_{\text{max}}$) method underestimates the average shell thickness by about 30%.

Finally, we present the linear value R_s of the shell radius as determined by phase-lag measurements (Herman and Habing 1985), the distance r obtained by combining R_s with the average angular radius $\langle \theta_s \rangle$ at V_0 , the total rate \dot{M} of mass loss obtained by using equation (14) of Herman, Burger, and

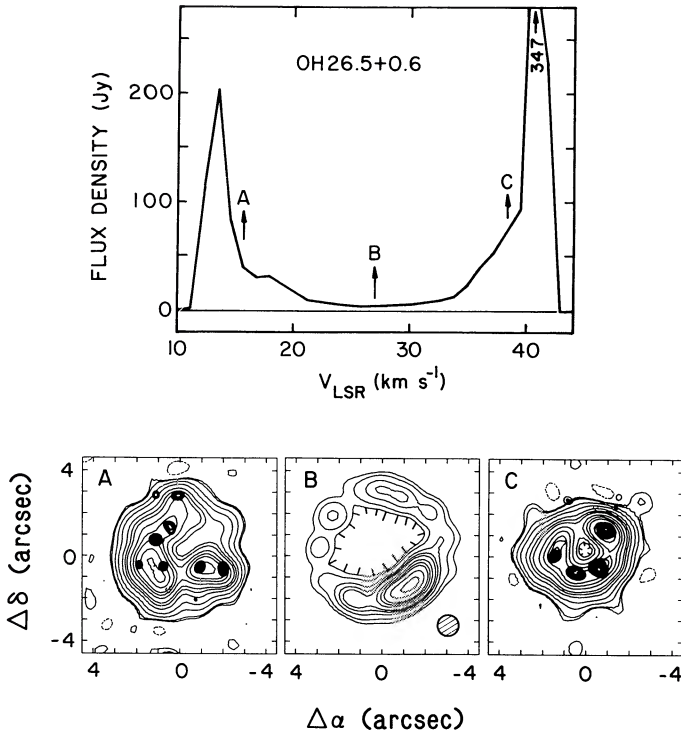


FIG. 6.—VLA spectral line profile and maps at selected velocities for OH 26.5+0.6. Maps A and C are superpositions of MERLIN data (Diamond *et al.* 1985) onto the VLA maps from Fig. 5 at velocities of 15.6 and 38.4 km s⁻¹, respectively. Map C shows the emission within ±0.5 km s⁻¹ of the stellar velocity at 27.0 km s⁻¹. The origins of the maps are identical to that in Fig. 5, and the FWHM VLA beam is shown in the lower right corner of map B.

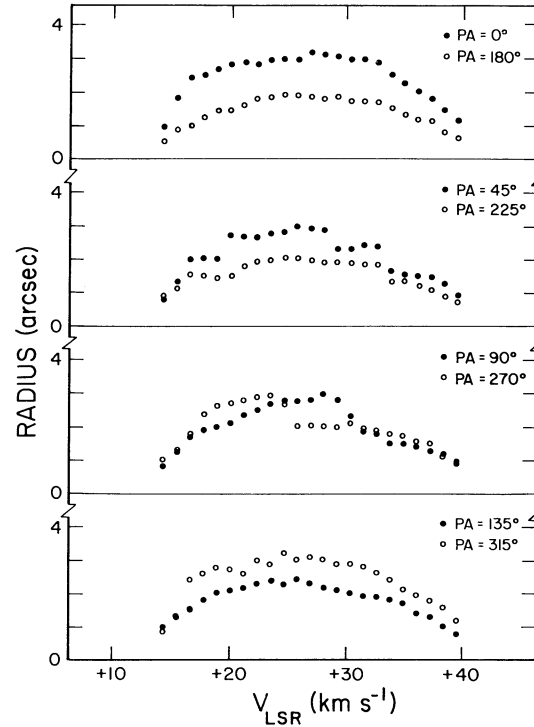


FIG. 8.—Angular distance θ of the maximum emission from the origin of the maps in Fig. 5 as a function of the position angle and radial velocity

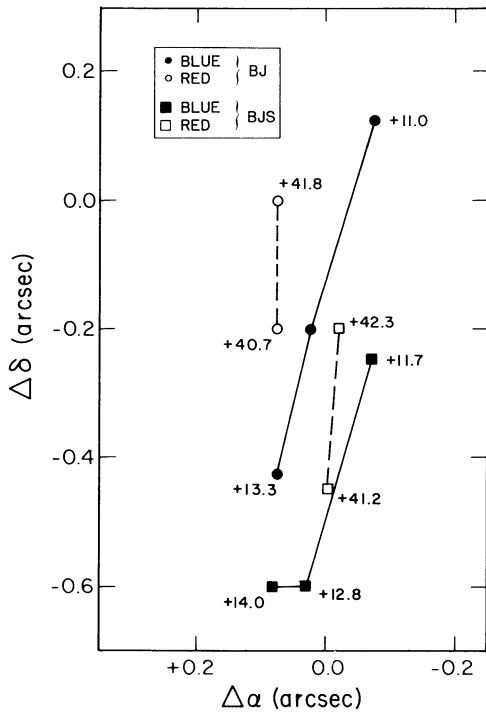


FIG. 7.—Absolute positions of emission components at the velocities of the peaks and at more extreme low or high velocities for OH 26.5+0.6. The data sets are BJ = this paper and BJS = Bowers, Johnston, and Spencer (1983). The origin of the maps is identical to that in Fig. 5.

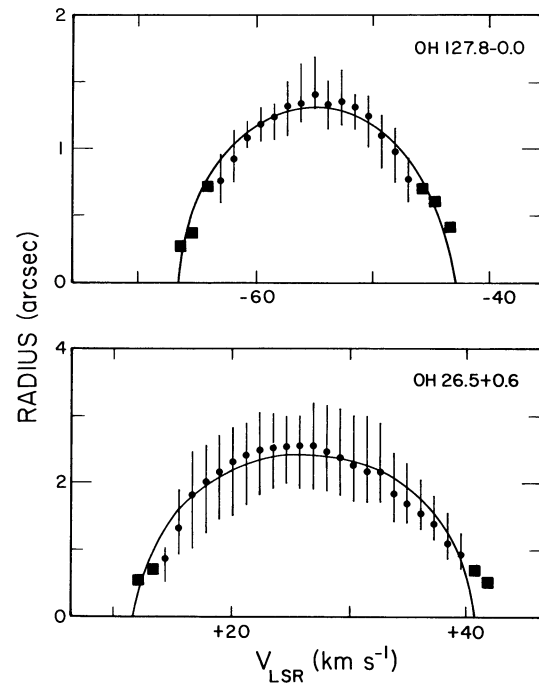


FIG. 9.—Angular distance θ of the maximum emission from the adopted stellar position as a function of radial velocities. Filled circles represent values averaged over 16 equally spaced position angles; boxes represent values obtained from the visibility curves. Vertical bars indicate the minimum and maximum values at any position angle. Curves show the least-squares fits of eq. (1) to the data.

TABLE 2
DETERMINATION OF SHELL PARAMETERS

Parameter	OH 127	OH 26.5	Method
V_0 (km s ⁻¹)	-54.9 ± 0.2	27.0 ± 0.1	V^W
	-54.7 ± 0.2	27.0 ± 0.1	V^P
	-54.9 ± 0.1	26.3 ± 0.4	Least-squares fit
V_e (km s ⁻¹)	12.0 ± 0.2	15.1 ± 0.1	V^W
	11.1 ± 0.2	13.9 ± 0.1	V^P
	11.5 ± 0.2	14.4 ± 0.2	Least-squares fit
θ_s (") ^a	1.38 ± 0.14	2.56 ± 0.51	θ_s vs. P.A.
	1.29 ± 0.04	2.39 ± 0.06	Least-squares fit
$\Delta\theta_s$ (rms)/ $\langle\theta_s\rangle$	0.10	0.20	θ_s vs. P.A.
$\theta_o - \theta_i$ (") ^a	0.86 (P.A. = 90°)	0.86 (P.A. = 225°)	2 × FWHM
	...	1.70 (P.A. = 270°)	2 × FWHM
	0.5	1.3	(θ_{\min} , θ_{\max})
θ_o/θ_i (= R_o/R_i)	1.91 (P.A. = 90°)	1.58 (P.A. = 225°)	2 × FWHM
	...	2.48 (P.A. = 270°)	2 × FWHM
	1.4	1.7	(θ_{\min} , θ_{\max})
R_s (AU)	8573 ± 480	2193 ± 173	Phase lag
r (kpc)	6.21 ± 1.0	0.86 ± 0.2	R_s , $\langle\theta_s\rangle$
\dot{M} (M_\odot yr ⁻¹)	8.0×10^{-5b}	3.1×10^{-5}	IR modeling
$\langle L \rangle$ (L_\odot)	3.0×10^5	1.1×10^4	IR fluxes

^a 1" = 6212 AU for OH 127; 1" = 857 AU for OH 26.5.

^b See § IVc.

Penninx (1986) with an assumed gas-to-dust ratio of 160 (Knapp 1985), and the time-averaged bolometric luminosity at the inferred distance (also from Herman, Burger, and Penninx).

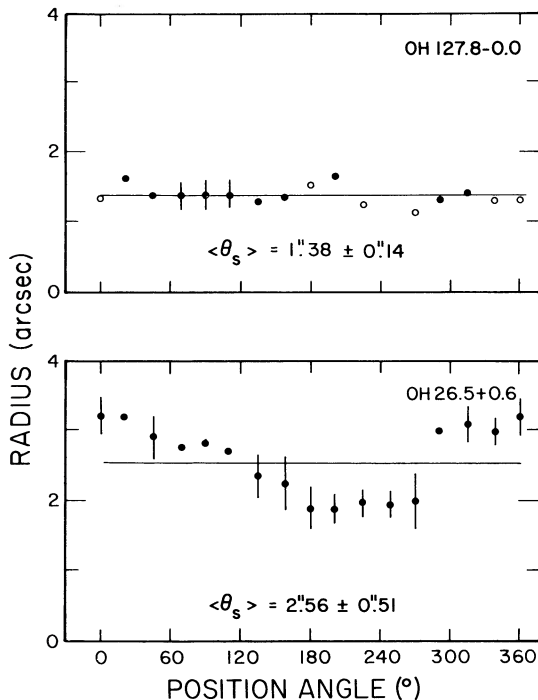


FIG. 10.—Angular radius θ of the maximum emission from the adopted stellar position as a function of position angle. Filled circles represent values measured at $V = V_0$. Empty circles represent values measured within 3 km s^{-1} of V_0 . Vertical bars indicate the FWHM shell thickness after deconvolution from the beam.

IV. DISCUSSION

In the previous section, we have attempted to determine the stellar positions and shell parameters with the standard expanding shell model. The data now available for OH 127 and OH 26.5 are of high quality, not seriously limited by the spectral sensitivity, dynamic range, or velocity resolution. Our results therefore provide an estimate of the highest level of accuracy determinable for the case where the assumptions of the standard model are used to estimate the shell parameters. We estimate the *optimum* uncertainties to be as follows: stellar position ($\pm 0.05\theta_s$), V_0 ($\pm 0.1 \text{ km s}^{-1}$), V_e ($\pm 0.5 \text{ km s}^{-1}$), R_o/R_i ($\pm 30\%$), $\langle\theta_s\rangle$ ($\pm 10\%$), and r ($\pm 15\%$).

For the most part, deviations of the shell structure from the assumptions of the standard model dominate these uncertainties and cause significant differences between the observed and predicted $\theta(V)$ relationships. In this section, we examine the possible nature and magnitude of these deviations in an effort to understand the relative extent to which they may be products of the mass-loss process or of the ambient interstellar environment.

a) Shell Geometry

i) OH 127

Approximate positional coincidence of peak features and roughly circular ringlike structures have led various authors to conclude that the OH shells of many OH/IR stars are approximately spherical at large ($R > 1000 \text{ AU}$) radii (BJS; Herman *et al.* 1985). In contrast, there appear to be frequent indications of axisymmetric shell structure for smaller ($R < 500 \text{ AU}$) OH shells associated with Mira variables (BJdV). The latter authors suggest that these results can be reconciled if the OH is distributed in radially expanding ellipsoidal shell structures which are a consequence of axisymmetric outflow. For such a geometry, evidence for axisymmetry will be more subtle for the

larger shells unless the degree of axisymmetry is high, because the emission from the larger shells is stronger and amplifies linearly rather than exponentially. At a given radial velocity, there is less contrast between the output intensities at different position angles on the sky, resulting in an approximately circular or slightly elliptical map structure with a nonuniform brightness distribution, which can appear as large-scale clumpy features in VLA maps.

The shell radius of OH 127 is constant to within about $\pm 10\%$ on the near (approaching) and far (receding) sides of the shell (Fig. 9) and at the stellar velocity (Fig. 10), making this star one of the best-known examples with an approximately spherical OH shell. It is therefore instructive to determine the upper limit for any ellipticity e . Respectively defining a and b as the semimajor and semiminor axes perpendicular to the line of sight, we find from Figure 10 that $a \leq 1'.38 + 0'.14$, $b \geq 1'.38 - 0'.14$, $a/b \leq 1.23$, and $e \leq 0.58$. There is also a hint of a double sine wave in the upper panel of Figure 10, possibly suggesting a major axis oriented toward the position angles of 20° and 200° . The two brightest clumps in Figure 2c therefore may represent slightly larger column densities close to the minor axis. It is clear that data with very high quality are necessary to establish stronger quantitative constraints on the geometry of the shell. The available data do not rule out a significant degree of axisymmetry for the outflow of this star.

ii) OH 26.5

As noted in § IIIb, the shell structure of OH 26.5 is strongly asymmetric. Figure 10 shows that the angular radius at the stellar velocity varies from about $2''$ to $3''$, depending on the position angle. Figure 8 shows no indication that the asymmetry is caused by substantially different outflow velocities in different directions. Since OH at large radii in the envelopes is thought to be produced by ultraviolet photodissociation of H_2O (Huggins and Glassgold 1982; Netzer and Knapp 1987), a more likely cause for the asymmetry is anisotropic UV radiation from the interstellar environment.

Using the catalog of O-type stars by Garmany, Conti, and Chiosi (1982), which is estimated to be complete to about 2.5 kpc, BJS found three O stars within 2° of OH 26.5 but were unable to conclude that they affected its shell structure because of the large uncertainty for the distance of OH 26.5. Our revised estimate of 860 ± 200 pc is now comparable to the distance of 1 kpc estimated by Garmany, Conti, and Chiosi for the O8 star BD $-6^\circ 4787$. Assuming both stars are at a distance of 1 kpc, the O star is located about 24 pc from OH 26.5 at a position angle of 235° , and its UV contribution at 1025 \AA is estimated to be comparable to the ambient value (BJS).

According to the photodissociation models, the effect of the O star will be to produce a larger density of OH molecules at a smaller radius, accounting for both the asymmetry of the shell and the brighter clump of emission seen to the southwest in Figure 6b. Adopting \dot{M} and V_e from Table 2 and using equation (12) of Netzer and Knapp, we find an OH shell radius of about $3''$ for an ambient radiation field characteristic of the galactic plane. This computed radius agrees very well the value observed at P.A. $\approx 0^\circ$ in Figure 10. The smaller radius at P.A. $\approx 235^\circ$ then indicates a radiation field about 50% larger than the ambient value.

b) Velocity Structure

In addition to asphericity of the shell, deviations of its structure from the assumptions of the standard model can be

induced by several kinematic components. In this section, we consider the upper limits to such components.

i) Rotation

Significant rotation is not expected at large radii in the circumstellar envelopes of late-type stars, but some rotation may be present due to the phenomenon of magnetically enforced corotation. Bieging and Nguyen-Q-Rieu (1988) suggest this possibility to explain a small (1.2 km s^{-1}) rotational component at a distance of 3700 AU in the envelope of CRL 2688. Strong magnetic fields are known to exist in Mira stars and cool supergiants (Barvanis, McIntosh, and Predmore 1987) and may contribute to their axisymmetric shell structure (BJdV), so we cannot *a priori* dismiss the possibility of small rotational components. Additionally, a large rotational component might occur if the system is a close binary (Kahane, Maizels, and Jura 1988).

The angular distribution of masers produced by a radial outflow in which there is a rotational component has been considered by BJdV. Inspection of their Figures 19 and 20 shows that a rotational component will shift the velocity of the maximum angular shell radius away from the stellar velocity, where the exact amount depends on the rotation law, the shell thickness, and the inclination of the plane of rotation to the line of sight. This result can be used to obtain a crude upper limit to a rotational component if values of the angular radius θ are obtained throughout the velocity range of the envelope. For example, the $\theta(V)$ curves for OH 26.5 (Fig. 8) show that the largest values of θ occur near the stellar velocity for position angles of 0° and 180° but are shifted away from it by ± 2 or 3 km s^{-1} at position angles of 90° and 270° . If this shift is caused by rotation, then the projected axis of rotation is oriented along the north-south direction, the line-of-sight rotational component is $\leq 3 \text{ km s}^{-1}$, and the ratio of rotational to radial components is ≤ 0.2 . It remains to be seen whether rotation is present in this or any other OH shell, because asymmetry of the shell geometry complicates the interpretation.

ii) Radial Acceleration

From analysis of the outflow velocity as a function of radius in the envelope of VX Sgr, Chapman and Cohen (1986) suggest evidence for radial acceleration at a large distance from the supergiant. In the region of the 1612 MHz masers ($R = 1400$ AU) they find $\epsilon \approx 0.2$, where $\epsilon = (d \ln V)/(d \ln R)$. Other possible indications of increasing outflow velocity at radii ≥ 1000 AU are provided by Bowers (1984) for the supergiant IRC +10420 ($\epsilon \approx 0.2$) and by BJdV for the Mira variables R Aql ($\epsilon = 0.09$) and IK Tau ($\epsilon = 0.07$). Netzer (1989) has proposed that radial acceleration at large distances may be a common phenomenon for thick envelopes.

None of the maser shells for the aforementioned stars have emission distributed uniformly throughout a spherical region, so derived values of ϵ must be regarded with caution, since the outflow velocity indicated by the maser emission may be less than the actual outflow velocity because of projection effects along the line of sight. In contrast, the emission for OH 127 and OH 26.5 is fairly uniformly distributed throughout 4π sr relative to the star. An upper limit for the value of ϵ can thus be obtained by combining information from the profile structure with our direct measurements of the shell thickness (Table 2). By assuming that the outflow velocities at the inner and outer radii of the maser shell are given respectively by V_e^P and V_e^W , we find $\epsilon \leq 0.12$ for OH 127 ($R_o/R_i = 1.9$) and $\epsilon \leq 0.14$ for OH 26.5 ($R_o/R_i \approx 2$). These upper limits are the first to be derived

for OH/IR stars and are consistent with the values found for Miras.

iii) Velocity Fluctuations

Random velocity fluctuations (turbulence) might be introduced by the mass ejection process, by interaction of the outflowing gas with the interstellar gas, or by energy input from hot stars or supernovae. Possible indicators of such fluctuations are the small-scale (<0.3) angular structures seen in Figures 2 and 6 (Deguchi 1982), the presence of emission outside the velocity range of the peak profile features (BJS; Diamond *et al.* 1985), and relatively large FWHM widths of the peak features (Alcock and Ross 1986). Comparison of values of V_e^P and V_e^W in Table 2 suggest fluctuations ≤ 2 km s^{-1} ; a comparable value is obtained from the FWHM widths of the peak profile features in Figures 2 and 6.

c) The $\Delta V - L$ Relation

Based on the inferred distance r to OH 127 given in Table 2, the time-averaged bolometric luminosity exceeds the limiting luminosity of an asymptotic giant branch star by a factor of about 5, indicating that OH 127 is a helium core-burning supergiant. That distance is based on the phase-lag radius and the mean angular radius $\langle\theta_s\rangle$. If we instead compute r by using the outer radius of the OH shell ($\theta_o = 1.81$ from Table 2), we find that the luminosity still exceeds the maximum by a factor of 3. To investigate further the possible supergiant nature of this star, we estimate the kinematic distance r_k from the rotation curve of Brand (1986), which is thought to be the best available representation for the outer Galaxy (L. Blitz, private communication). Assuming a velocity dispersion of 10 km s^{-1} for supergiants, we obtain $r_k \approx 8.4 \pm 1$ kpc, where the error is determined by computing r_k at $V = V_o \pm 10$ km s^{-1} . The agreement of r and r_k is sufficient to suggest that OH 127 is indeed a supergiant, unless, for example, the correction for interstellar extinction needed to estimate the bolometric flux is severely underestimated.

It is well known that the velocity separation ΔV of the peak OH emission features tends to be larger (≥ 40 km s^{-1}) for optically identified OH supergiants than for most OH Miras and OH/IR stars (Bowers and Kerr 1978, and references therein). The possibility that ΔV is a luminosity indicator is supported by Baud *et al.* (1981), who show that the galactic distribution of OH/IR stars with large values of ΔV indicates a younger population than the distribution of stars with small ΔV . However, Jones (1987) demonstrates that the correlation of ΔV with L is not as firm as previously thought.

OH 127 provides an excellent counterexample of the $\Delta V - L$ relation. Its value of ΔV (22 km s^{-1}) is much less than for known supergiants and is also less than the value of 28 km s^{-1} for OH 26.5 whose estimated luminosity is about 27 times smaller. Moreover, the OH light curves for OH 127 and OH 26.5 are similar to each other and significantly different than the small-amplitude, semiregular light curves of the well

known supergiants NML Cyg and VY CMA (Herman and Habing 1985). It thus appears that neither the OH profile shape nor the light curve shape is a foolproof indicator of the stellar luminosity.

The values of ΔV and OH luminosity for OH 127 are comparable to those for the OH supergiant discovered in the Large Magellanic Cloud by Wood, Bessell, and Whiteoak (1986). Those authors suggest that smaller values of these quantities may be caused by a low metal abundance, in which case the dust opacity is smaller than normal and there is less radiative acceleration of the outflowing material. Evidence that the metallicity decreases in the anticenter direction of the Galaxy (Jura, Joyce, and Kleinmann 1989) supports a similar explanation for OH 127, in which case the assumed gas-to-dust ratio and derived rate of mass loss in § IIIc may be too small. If, for example, the rate of momentum $\dot{M}V_e$ in the mass outflow is equal to the rate L/c in the stellar radiation field, then $\dot{M} = 5.7 \times 10^{-4} M_\odot \text{ yr}^{-1}$ and the appropriate gas-to-dust ratio is about 1150.

V. CONCLUSION

A comparison of VLBI, MERLIN, and VLA data for OH 127.8-0.0 shows that this OH/IR star is one of the best-known examples which conforms to the predictions of the standard expanding shell model. Within ± 3 km s^{-1} of the stellar velocity, a clumpy but approximately circular shell is seen with an ellipticity $e \leq 0.58$. The linear shell radius is constant to within about $\pm 10\%$ (rms) on the near and far sides of the shell and at the stellar velocity. The highest degree of geometric symmetry occurs at the position of the compact VLBI component seen in the low-velocity peak feature, supporting the possibility that this component may be amplifying the thermal emission from the stellar photosphere.

A similar comparison of data for OH 26.5+0.6 shows a more asymmetrically shaped shell whose radius in different directions from the star differs by as much as 50%. At the stellar velocity, the radius is smallest in the direction of an O8 star which is at a comparable distance and whose UV radiation field may be producing the shell asymmetry. An upper limit of 3 km s^{-1} is derived for any line-of-sight rotational component in the OH maser region of OH 26.5, and upper limits also are determined for the amount of radial acceleration ($\epsilon \leq 0.1$) and random velocity fluctuations (≤ 2 km s^{-1}) in the maser shells of these two OH/IR stars. Accurate distances ($\Delta r \approx \pm 20\%$) are determined for both stars. The bolometric luminosity of OH 127 indicates that it is a helium core-burning supergiant, although its OH profile structure and light curve shape are similar to those of asymptotic giant branch stars.

We thank the National Radio Astronomy Observatory for providing observing time for this project and M. Jura for useful comments.

REFERENCES

- Alcock, C., and Ross, R. R. 1986, *Ap. J.*, **305**, 837.
 Andersson, C., Johansson, L. E. B., Goss, W. M., Winnberg, A., and Nguyen-Quang-Rieu. 1974, *Astr. Ap.*, **30**, 475.
 Barvanis, R., McIntosh, G., and Predmore, C. R. 1987, *Nature*, **329**, 613.
 Baud, B. 1981, *Ap. J. (Letters)*, **250**, L79.
 Baud, B., Habing, H. J., Matthews, H. E., and Winnberg, A. 1981, *Astr. Ap.*, **95**, 156.
 Bieging, J. H., and Nguyen-Quang-Rieu. 1988, *Ap. J.*, **324**, 516.
 Booth, R. S., Kus, A. J., Norris, R. P., and Porter, N. D. 1981, *Nature*, **290**, 382.
 Bowers, P. F. 1984, *Ap. J.*, **279**, 350.
 ———. 1985, in *Mass Loss from Red Giants*, ed. M. Morris and B. Zuckerman (*Ap. Space Sci. Lib.*, **117**, 189).
 Bowers, P. F., and Johnston, K. J. 1985, unpublished (BJ85).
 Bowers, P. F., Johnston, K. J., and de Vegt, C. 1989, *Ap. J.*, **340**, 479 (BJdV).
 Bowers, P. F., Johnston, K. J., and Spencer, J. H. 1981, *Nature*, **291**, 382.
 ———. 1983, *Ap. J.*, **274**, 733 (BJS).

- Bowers, P. F., and Kerr, F. J. 1978, *A.J.*, **83**, 487.
 Bowers, P. F., Reid, M. J., Johnston, K. J., Spencer, J. H., and Moran, J. M. 1980, *Ap. J.*, **242**, 1088; erratum **248**, 880.
 Brand, J., 1986, Ph.D. thesis, University of Leiden.
 Chapman, J. M., and Cohen, R. J. 1986, *M.N.R.A.S.*, **220**, 513.
 Deguchi, S. 1982, *Ap. J.*, **259**, 634.
 Diamond, P. J., Norris, R. P., Rowland, P. R., Booth, R. S., and Nyman, L.-Å. 1985, *M.N.R.A.S.*, **212**, 1.
 Elitzur, M., Goldreich, P., and Scoville, N. 1976, *Ap. J.*, **205**, 384.
 Garmany, C. D., Conti, P. S., and Chiosi, C. 1982, *Ap. J.*, **263**, 777.
 Herman, J., Baud, B., Habing, H. J., and Winnberg, A. 1985, *Astr. Ap.*, **143**, 122.
 Herman, J., Burger, J. H., and Penninx, W. H. 1986, *Astr. Ap.*, **167**, 247.
 Herman, J., and Habing, H. J. 1985, *Astr. Ap. Suppl.*, **59**, 523.
 Huggins, P. J., and Glassgold, A. E. 1982, *A.J.*, **87**, 1828.
 Jones, T. J. 1987, in *Late Stages of Stellar Evolution*, ed. S. Kwok and S. R. Pottasch (*Ap. Space Sci. Lib.*, **132**, 3).
 Jura, M., Joyce, R. R., and Kleinmann, S. G. 1989, *Ap. J.*, **336**, 924.
 Kahane, C., Maizels, C., and Jura, M. 1988, *Ap. J. (Letters)*, **328**, L25.
 Knapp, G. R. 1985, *Ap. J.*, **293**, 273.
 Kwok, S. 1976, *J.R.A.S. Canada*, **70**, 49.
 Netzer, N. 1989, *Ap. J.*, **342**, 1068.
 Netzer, N., and Knapp, G. R. 1987, *Ap. J.*, **323**, 734.
 Norris, R. P., Booth, R. S., Diamond, P. J., Nyman, L.-A., Graham, D. A., and Matveyenko, L. I. 1984, *M.N.R.A.S.*, **208**, 435.
 Norris, R. P., Diamond, P. J., and Booth, R. S. 1982, *Nature*, **299**, 131.
 Reid, M. J., Muhleman, D. O., Moran, J. M., Johnston, K. J., and Schwartz, P. R. 1977, *Ap. J.*, **214**, 60.
 Sun, J., and Kwok, S. 1987, *Astr. Ap.*, **185**, 258.
 Szymczak, M. 1987, *Ap. Space Sci.*, **139**, 63.
 Welty, A. D., Fix, J. D., and Mutel, R. L. 1987, *Ap. J.*, **318**, 852.
 Wood, P. R., Bessell, M. S., and Whiteoak, J. B. 1986, *Ap. J. (Letters)*, **306**, L81.

P. F. BOWERS and K. J. JOHNSTON: Code 4130, Naval Research Laboratory, Washington, DC 20375